A Cytotoxic Indazole-based Gold(III) Carboxamide Pincer Complex Targeting DNA Through Dual Binding Modes of Groove Binding and Alkylation

Rufaro Razuwika,*[a] Sheldon Sookai,[a] Ruth Aronson,[b] Mandeep Kaur,[b] and Orde Q. Munro[a, c]

Gold(III) complexes have garnered increasing attention in drug delivery due to their structural and mechanistic similarities to cisplatin. This study investigates an indazole-based gold(III) carboxamide pincer complex, [$N^2 \cdot N^6$-bis(1-methyl-^{1}H-indazol-3-yl)pyridine-2·6-dicarboxamide]gold(III) chloride (**AuL**), for its potential as an anticancer agent. Speciation analysis at physiological pH revealed that **AuL** predominantly exists as a neutral chlorinated species. The complex exhibited strong cytotoxicity against the MCF-7 breast cancer cell line, with an impressive IC$_{50}$ value of 9 μM, while showing no significant activity against the HT-29 colon cancer cell line. Comprehensive analysis using electrophoresis, viscometry, ultraviolet-visible spectroscopy (UV-Vis), circular dichroism (CD), linear dichroism (LD) spectroscopy, and biomolecular simulations demonstrated that **AuL** binds to DNA via a dual mechanism, specifically minor groove binding and alkylation, with binding constants $K_{a1} = 1.48 \times 10^9$ M^{-1} and K$_{a2}$ = 6.59 × 10^5 M^{-1}, respectively. Our data indicate that **AuL** initially binds to the minor groove of DNA, at which point a nucleobase substitutes the Cl ion, resulting in **AuL** binding directly to the DNA bases. In conclusion, the dual binding mode of **AuL** with DNA underscores its potential as a promising anticancer agent, opening new avenues for drug discovery and the development of metal-based therapeutics.

1. Introduction

Gold(III) pincer complexes are attracting significant interest as potential anticancer agents due to the gold(III) ion's isoelectronic and isostructural similarity to platinum(II), the central metal ion in cisplatin, the most widely used and successful anticancer metallodrug to date.[1,2] Recent studies have demonstrated that certain gold(III) complexes exhibit in vitro cytotoxicity against specific cancer cell lines, with activity levels that are comparable to or even exceed those of cisplatin.[1–3] Ongoing research continues to explore the therapeutic potential of gold(III) complexes, aiming to expand the arsenal of effective metal-based anticancer agents.[4–6]

Despite advancements in the study of gold(III) complexes, further research is necessary, particularly on pincer complexes to better understand their stability, reactivity, and therapeutic potential, given the limited number of available libraries for these molecules. A common strategy to enhance cytotoxicity involves modifying these complexes with moieties known for their anticancer properties. One such group is the indazole moiety, a purine base analog,[7,8] which has recently gained prominence as a key building block in pharmaceutical and medicinal chemistry. [8–10] Although rare in nature, synthetic indazole derivatives have demonstrated diverse pharmacological properties, including anti-inflammatory, analgesic, antiarrhythmic,[10] antibacterial,[11] anti-fungal[12] anti-HIV[13–19] Furthermore, several indazole-based drugs have shown success in cancer treatment,[20–32] leading to the exploration of novel indazole motifs for next-generation therapeutics.[8] Consequently, the indazole group and its bioisosteres remain a major focus of extensive studies.[9,33–35]

Several carboxamide pincer complexes have been reported, though only a few feature gold(III) as the central metal ion.[36–38] These complexes incorporate amide groups, which are prevalent in DNA, cellular proteins,[39,40] and numerous pharmaceutical drugs.[39,41] Amide functionalities in these complexes contribute to hydrogen bonding, enhancing their rigidity and stability.[42,43]

DNA is a primary molecular target in cancer therapy due to its essential role in cellular functions. Disrupting DNA integrity has been shown to impair the activity of cancerous cells, making it a critical focus for treatment strategies.[44–46] By binding to DNA and disrupting its secondary and tertiary structures, drugs can effectively inhibit uncontrolled cell replication. This

[a] R. Razuwika, S. Sookai, O. Q. Munro
Molecular Sciences Institute, School of Chemistry, University of the Witwatersrand, 1 Jan Smuts Avenue, Johannesburg 2050, South Africa
E-mail: razuwika@gmail.com

[b] R. Aronson, M. Kaur
School of Molecular and Cell Biology, University of the Witwatersrand, 1 Jan Smuts Avenue, Johannesburg 2050, South Africa

[c] O. Q. Munro
School of Chemistry, University of Leeds, Woodhouse Lane, Leeds LS2 9JT, UK

Chemistry–A European Journal

Research Article
doi.org/10.1002/chem.202404345

Chemistry
Europe
European Chemical
Societies Publishing

inhibition is achieved through mechanisms such as alkylation, base displacement, intercalation, or groove binding.

Herein, we report the synthesis of an indazole-based carboxamide pincer ligand and its corresponding gold(III) complex, [N2·N6-bis(1-methyl-1H-indazol-3-yl)pyridine-2·6-dicarboxamide]gold(III) chloride (**AuL**). We hypothesize that **AuL** facilitates DNA binding through π-π stacking interactions between the indazole moiety and nucleic acid bases. This would engender significant, exploitable cytotoxicity for the complexes in vitro against the human breast adenocarcinoma cell line, MCF-7 and a human colorectal adenocarcinoma cell line, HT-29.

2. Results and Discussion

2.1. General synthesis and characterization

The ligand [N2·N6-bis(1-methyl-1H-indazol-3-yl)pyridine-2·6-dicarboxamide (**H₂L**), which has been reported by Razuwika and Munro,[47] was metalated by adapting and modifying a method by Akhmadullina, et al.[48] This entailed stirring **H₂L** with potassium tetrachloroaurate (KAuCl₄) in a binary mixture of water-acetonitrile (3:1) for 15 hours, to yield a novel carboxamide gold(III) pincer complex **AuL** (Figure 1a). The product was characterized using a range of analytical techniques, including nuclear magnetic resonance spectroscopy (NMR) and fourier transform infrared spectroscopy (FT-IR) spectroscopy, elemental analysis, as well as high-resolution mass spectrometry.

The NMR, FT-IR and electronic spectra of **AuL** are mainly presented to highlight the salient spectroscopic features of the synthesized compound. In Figure 1b, the 1H NMR spectrum reflects coordination of the gold(III) ion to the pincer ligand. In the 1H NMR spectrum of **H₂L**, the resonance at 12 ppm (peak *e*) disappears upon the complexation with the gold(III) ion in the spectrum of **AuL**, signifying successful metalation. This disappearance is attributed to the deprotonation of the amide protons in **H₂L**, which facilitated metal binding. Metalation of the ligand resulted in a general up field shift for all protons except proton *b* (at the meta position), which shifts downfield due to increased deshielding. The 13C NMR spectrum (Figure S1) supports the 1H NMR findings, showing the downfield shift of the amide carbonyl peak from 161.98 ppm in **H₂L** to 170.04 ppm in **AuL**, which is attributed to the higher electronegativity of Au in comparison to H. [49–51]

The FT-IR spectra (Figure 1c), show that the amide NH stretch (3310-3290 cm⁻¹) and NH bend (1560-1585 cm⁻¹) peaks present in **H₂L** disappear upon complexation with the gold(III) ion, consistent with metalation. Additionally, the C=O stretch observed at 1690–1700 cm⁻¹ in **H₂L** shifts to a lower wavenumber (1683-1692 cm⁻¹) presumably from back-donation of metal electron density into the antibonding MO of the amide groups.

2.2. Crystallography

The crystal structure of **H₂L** was previously reported.[47] Single crystals of **AuL** were obtained by slow diffusion of tert-butanol
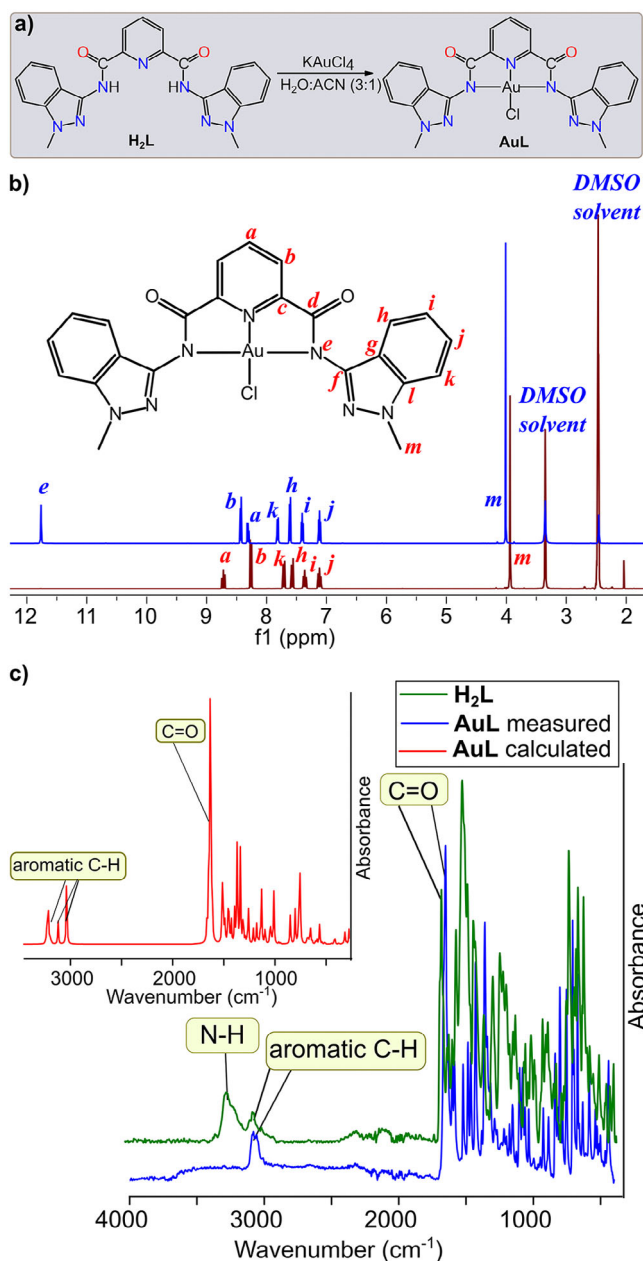

Figure 1. a) Structure and general synthetic scheme for the indazole based gold(III) carboxamide pincer complex **AuL** at room temperature for 15 hours under study.[48,52] b) A comparison between the proton NMR spectra for **H₂L** (blue) and **AuL** (red) displaying the presence and absence of the amide NH proton at 11.80 ppm. c) FT-IR spectra of **H₂L** and **AuL**, displaying the shift of the carbonyl peaks from 1692 to 1683 cm⁻¹ and the disappearance of the NH stretch and bend peaks at 1583 and 3316 cm⁻¹, respectively upon complexation with gold(III).

(tBuOH) into a DMSO solution of **AuL**, while single crystals of **AuLT** (a thymine derivative of **AuL**) were grown by slow diffusion of a thymine solution in water into a DMSO solution of **AuL**.

Unlike the carboxamide pincer ligand **H₂L**, which has been reported to exhibit atropisomerism,[47] the complex **AuL** does not display this property. The metal ion holds the pyridine and the amide nitrogen atoms, which are initially nonplanar, in a relatively planar configuration around the metal centre. While the anchoring site remains planar, the presence of a dihedral angle

Chemistry–A European Journal

Research Article
doi.org/10.1002/chem.202404345

**Chemistry
Europe**
European Chemical
Societies Publishing

allows the "pincer arms" to rotate. As a result, the complex crystallizes with C$_i$ symmetry. The rigidity imposed on the anchoring site reduces the flexibility of the compound, leading to the loss of atropisomerism.

Complexes **AuL** and **AuLT** crystallized in the P-1 space group. The coordination environment around the gold(III) ion is planar, however, the "indazole arms" of the pincer ligand deviate from the planarity of the central pyridine and AuN$_3$ coordination group with inequivalent dihedral angles of 60.1° and 56.5° in **AuL**. This distortion results in the loss of both chirality and C$_2$ symmetry in **AuL**, in distinct contrast to the precursor ligand **H$_2$L**.

AuLT provided important insights into the binding interactions of the thymine base with the gold(III) metal center. Thymine coordinates to the metal in its deprotonated ionic form, resulting in a neutral compound. The introduction of this aromatic group modifies the orientation of the "indazole arms" in **AuLT**, aligning them in the same direction, in contrast to **AuL**, where the arms are oriented oppositely. The dihedral angles between the indazole groups and mean plane passing through the central pyridine ring and AuN$_3$ coordination group are 86.7° and 89.2° in **AuLT**. While **AuL** exhibits nearly identical bond lengths for both Au—N$_{amide}$ bonds, **AuLT** shows a difference of 0.015 Å between these bonds (see Figure 2). This variation arises from the interactions depicted in Figure 2b, where the thymine group engages in π-π interactions with one of the indazole rings, thereby shortening the corresponding Au—N$_{amide}$ bond.

In general, the Au–N bond lengths are shorter in **AuLT** compared to those in **AuL**. The most significant change is observed between the Au–N$_{Thymine}$ (2.014 Å) and Au–Cl (2.265 Å) bonds, with a reduction of 0.251 Å upon the substitution of Cl$^-$ with thymine. This suggests that the Au–N bond is stronger than the Au–Cl bond, which is expected given that the anionic nitrogen is more basic than the chloride ion. The ability of nitrogen to donate a pair of electrons to the metal centre stabilizes the Au—N$_{thymine}$ bond. Thymine's bulkier structure compared to Cl$^-$ also increases the dihedral angles between the metal pincer core and the two "indazole arms" to ~90° in **AuLT**, compared to ~65° in **AuL** as noted above (Figure S5). This suggests that the pincer complex exhibits flexibility, allowing it to accommodate ligands of varying bulkiness. This adaptability could enhance the complex's ability to interact with a diverse range of molecules, potentially influencing its reactivity and stability.

2.2.1. Electronic spectroscopy

Preceding any spectroscopic studies, the gold(III) pincer complex **AuL** was electronically characterized in DMSO, and the ultraviolet-visible spectroscopy (UV-vis) absorption spectrum is presented in Figure 3. Three absorption maxima were identified at 267 nm ($\varepsilon = 9.05 \times 10^4$ M^{-1} cm^{-1}), 296 nm ($\varepsilon = 8.96 \times 10^3$ M^{-1} cm^{-1}), and 439 nm ($\varepsilon = 3.91 \times 10^3$ M^{-1} cm^{-1}). The peaks at 267 nm and 296 nm are attributed to the indazole rings, in accordance with data in the literature,[53,54] while the peak at 439 nm is characteristic of gold(III) complexes.[55] The transitions were further assigned using time-dependent density functional theory (TD-DFT) calculations at the HSEH1PBE/SDD level of theory. The DFT calculated electronic spectrum of **AuL** in DMSO (using a polar-
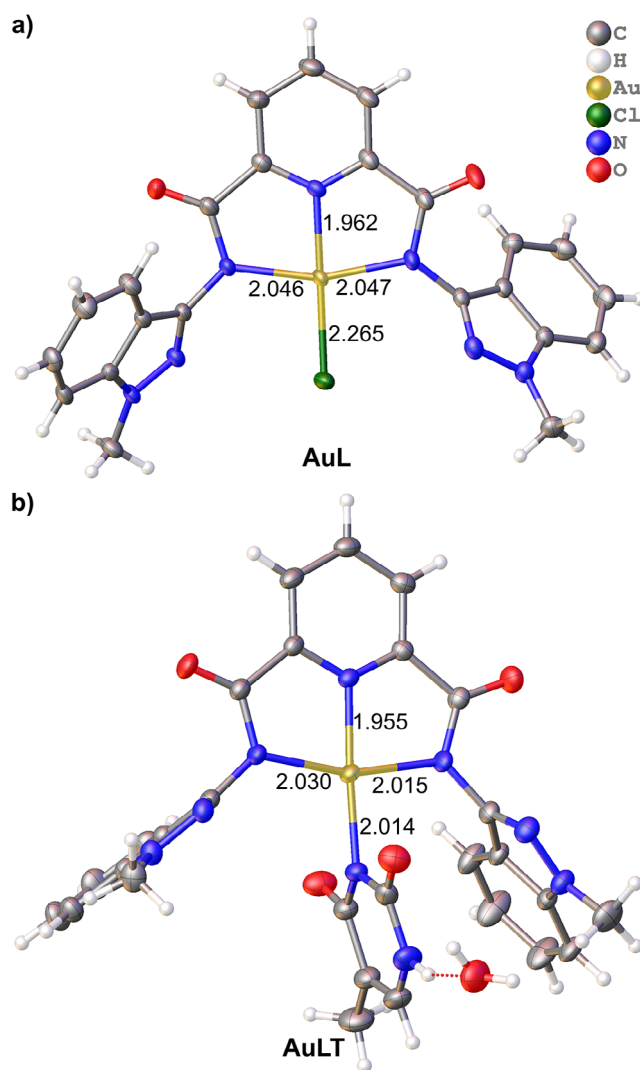

Figure 2. Selectively labelled views of the X-ray crystal structures of a) AuL and b) AuLT. Thermal ellipsoids are rendered at the 50% probability level and H atoms are drawn as spheres of an arbitrary radius. Space groups: P1$^-$. **AuL** and **AuLT** has C$_i$ symmetry.

izable continuum model) is shown in the inset to Figure 3a. The predicted absorption maxima and the major contributions to each transition are summarized in Figure 3b and Table S1. The calculated peaks correspond well with the experimental data after a wavelength adjustment of +30 nm.

The lower energy transition (378 nm), correlating with the experimental peak at 439 nm, involves excitation from the HOMO to the LUMO or LUMO+3. Higher energy transitions at 267 nm and 296 nm are assigned to excitations from the HOMO-9 to the LUMO+2, and from the HOMO-6 to the LUMO, respectively. The HOMO orbitals are π-bonding and delocalized across the indazole rings, while the LUMO and LUMO+3 are predominantly antibonding (π^*) in nature and localized on the gold metal centre. The LUMO+2 is primarily localized on the pyridine ring. The lowest energy transitions are thus attributed to intraligand charge transfer (ILCT) with a dominant $\pi \rightarrow \pi^*$ character. Due to the significant 5d$_{x^2-y^2}$ character in the LUMO, the
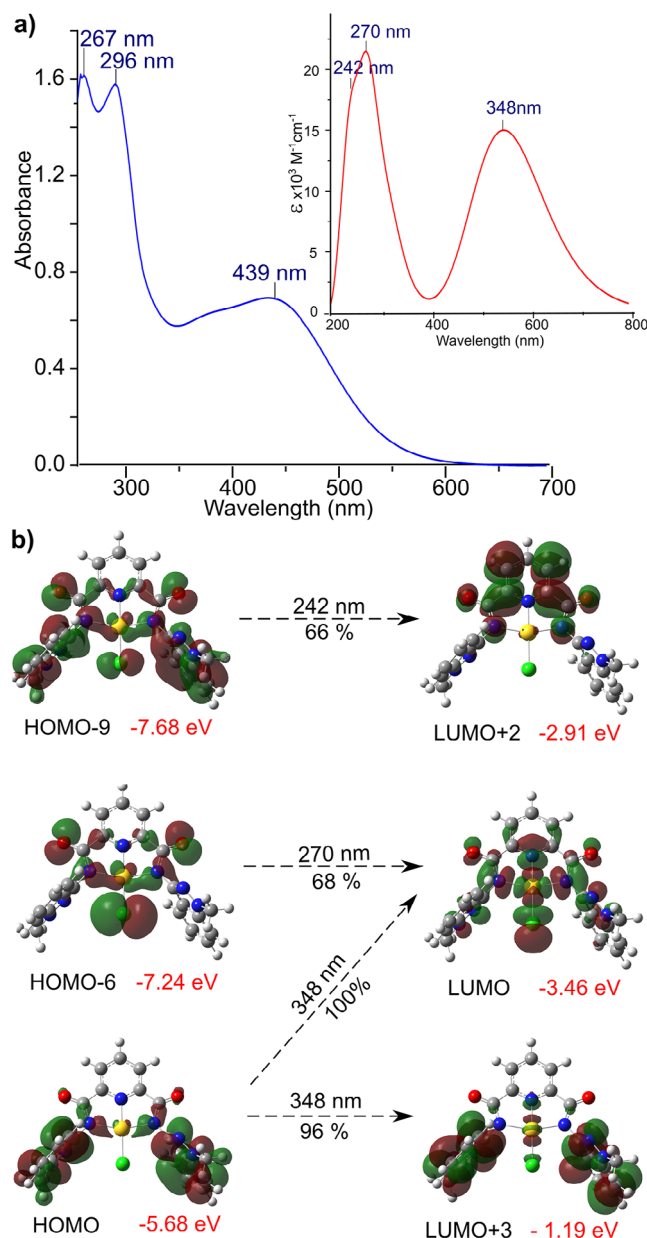
Chemistry–A European Journal

Research Article
doi.org/10.1002/chem.202404345

Chemistry
Europe
European Chemical
Societies Publishing

Figure 3. a) The experimental and DFT-calculated absorption spectra of **AuL** in DMSO, indicating the three absorption maxima lmax.The absorption envelope for the DFT-calculated spectrum is plotted with full width at half maximum intensity (FWHM) of 3000 cm-1. **b)** Molecular orbitals involved in the three most intense bands in the DFT-calculated electronic spectrum of **AuL** in DMSO. The percentage contribution of the electronic transitions to each band is indicated.

Figure 4. a) Electronic spectra of **AuL** at selected pH values in a multicomponent buffer maintained at constant ionic strength. b) The proposed scheme for changes in the structure of **AuL** with the increase in pH from 2–13. The pK$_a$ values for the speciation of AuL calculated using Equation 2 (illustrated in Figure S6), are indicated in the scheme.

HOMO-LUMO transition also includes a component of ligand-to-metal charge transfer (LMCT).

Notably, the LMCT band shifts are solvent and pH dependent. In DMSO (Figure 3a), a blue shift of this band is observed, likely due to the solvent's solvation effects that stabilizes higher energy states. However, in the multicomponent buffer (Figure 4a), where the pH range overlaps with that of DMSO (5-8), the LMCT band shifts to a lower wavelength, indicating a red shift. This difference may be due to the buffer's ionic interactions and specific solvation effects that stabilize lower
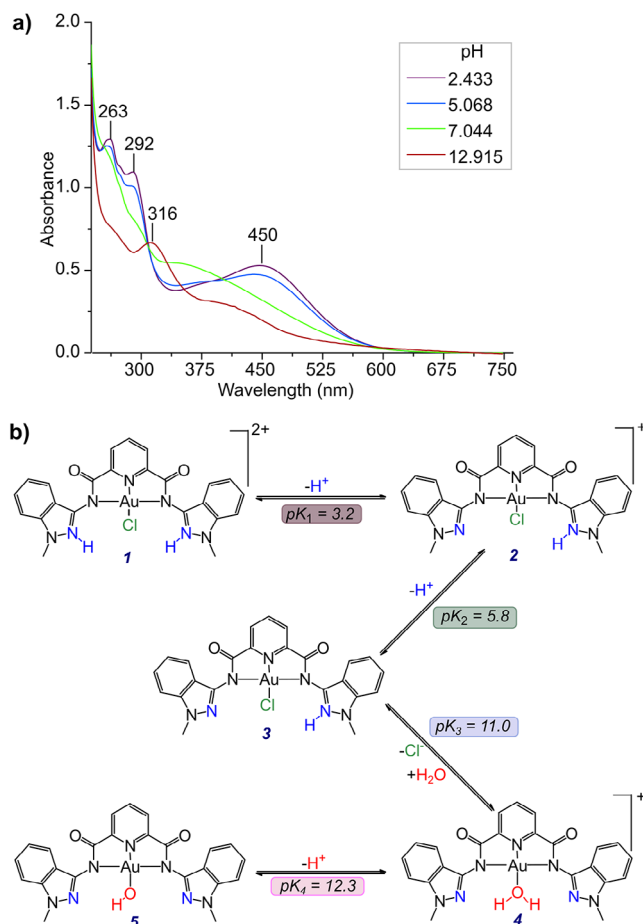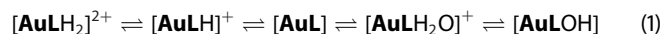
energy states. Additionally, increasing the pH causes a shift to a lower wavelength, likely due to protonation effects or changes in the coordination environment, further influencing the electronic transitions and absorption bands.

2.2.2. Speciation Studies

The identification of distinct chemical species at various pH levels is essential for understanding a compound's behaviour under physiological conditions.[56] In the context of **AuL**, it can be inferred that the number of species corresponds to the number of pK$_a$ values, with each pK$_a$ representing a transition point between two species and indicating an equilibrium shift.[57] This study aimed to: (i) determine which species of **AuL** is present at physiological pH (pH 7.4), conditions that closely mirror those encountered in biological systems[56,58] and (ii) accurately delineate the pK$_a$ of **AuL**. We therefore conducted a series of UV-vis spectroscopic measurements on **AuL** across a pH range of 2.433 to 12.915, closely monitoring alterations in the complex's electronic spectrum at 292, 330, and 460 nm, respectively (Figure 4). Even though physiological pH's range from 3.5 to 7.45, it is important to analyze the behaviour of **AuL** over a wide pH

Chem. Eur. J. **2025**, *31*, e202404345 (4 of 13)

© 2025 The Author(s). Chemistry – A European Journal published by Wiley-VCH GmbH

Chemistry–A European Journal

Research Article
doi.org/10.1002/chem.202404345

Chemistry
Europe
European Chemical
Societies Publishing

range to accurately delineate the complex's pK_a.[59] The titration data revealed the presence of four distinct transition points, corresponding to five different ionization states of **AuL** across the pH range, which allowed for the derivation of equations (1) and (2). The equations describe the speciation behaviour of **AuL** and offer valuable insights for further interpretation of the experimental data.

$$[\textbf{AuL}H_2]^{2+} \rightleftharpoons [\textbf{AuL}H]^+ \rightleftharpoons [\textbf{AuL}] \rightleftharpoons [\textbf{AuL}H_2O]^+ \rightleftharpoons [\textbf{AuL}OH] \quad (1)$$

Equation (1) reflects the dynamic equilibrium involving the different species of **AuL** as a function of pH and enables a quantitative understanding of how the concentration of each species changes with variations in pH. The four steps in the overall equilibrium are described by the equilibrium constants K_1, K_2, K_3, and K_4 for the forward reactions from left to right.

If the respective contributions of the species $[\textbf{AuL}H_2]^{2+}$, $[\textbf{AuL}H]^+$, $[\textbf{AuL}]$, $[\textbf{AuL}H_2O]^+$, and $[\textbf{AuL}OH]$ to the total absorbance (A_T) in a solution at various pH levels are A_A, A_B, A_C, A_D, and A_E, then equation for A_T is illustrated in equation (2) below. (The full derivation is given in the ESI.)

$$A_T = \frac{\alpha}{\beta}$$

where:

$$\alpha = A_A \times 10^{-4pH} + K_1 A_B \times 10^{-3pH} + K_1 K_2 A_C \times 10^{-2pH}$$
$$+ K_1 K_2 K_3 A_D \times 10^{-pH} + K_1 K_2 K_3 K_4 A_E$$

$$\beta = 10^{-4pH} + K_1 \times 10^{-3pH} + K_1 K_2 \times 10^{-2pH}$$
$$+ K_1 K_2 K_3 \times 10^{-pH} + K_1 K_2 K_3 K_4 \quad (2)$$

To provide a mechanistic understanding of the observed behaviour of the ionization state of **AuL** at different pH levels, the pK_a values were calculated using equation (2) in OriginPro 2023b.[60] The calculated pK_a values associated with each ionization state were found to be 3.2, 5.8, 11.0, and 12.3. Peak maxima at 263 nm and 291 nm are characteristic of the indazole ring,[53,54] while the maximum at 448 nm is characteristic of the gold(III) metal ion. The pH titration data revealed a red shift in the peak maxima at 263 and 291 nm, between pH's 2 and 5, indicating that the primary changes within this pH range occur on the indazole rings. At more alkaline pH levels, the main spectral changes are centred around 428 nm, which is characteristic of the gold(III) MLCT (metal-to-ligand charge transfer) transitions.

The proposed ionization of **AuL** from pH 2.433 to 12.915 is illustrated in Figure 4b. At acidic pH levels, the indazole rings undergo protonation, and the resulting species carries an overall charge of +2. As the pH increases to 3.2, one of the indazoles is deprotonated, altering the molecule's charge to +1. At pH 5.8, the second indazole ring undergoes deprotonation, yielding a neutral compound. At pH 11.0, an ion exchange occurs between Cl^- and H_2O, resulting in the molecule carrying a charge of +1. Finally, at pH 12.3, the water molecule is deprotonated, returning the complex to a neutral state. Based on the collected
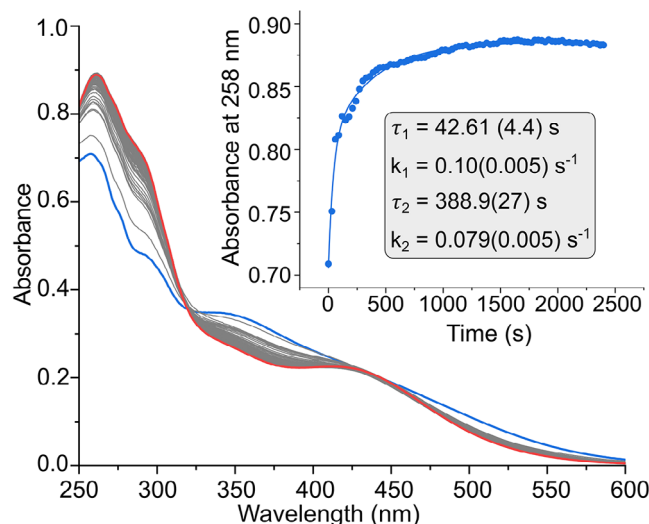

Figure 5. Electronic absorption spectra of 40 μM **AuL** in a water (10% V/V) and DMSO mixture containing GSH at a molar ratio of 1:1 [**AuL**]:[GSH]. The inset shows the change in absorbance at 258 nm as a function of time. The data are fitted to a standard double exponential kinetic function, $= K_1 e^{-x/t_1} + K_2 e^{-x/t_2} + A_\infty$, where k_1 and k_2 are adjustable pre-exponential factors, t_1 and t_2 are the time constants, and A_∞ the limiting absorbance.

data, it can be inferred that under physiological conditions, **AuL** predominantly exists as a neutral species *3* in Figure 4b.

2.2.3. Stability of AuL to reduction

Glutathione (GSH) serves a crucial role as the major component of the intracellular antioxidant system.[61] One of its main functions is the detoxification of heavy metal complexes within cells. With GSH concentrations ranging between 1 and 10 mM in cells, it is imperative to assess the stability of **AuL** in the presence of the intracellular reductant GSH. In this study, the reaction between GSH and **AuL** was investigated to estimate the stability of **AuL** under physiological GSH concentrations.[62,63]

The reaction of **AuL** and GSH was monitored over time by electronic spectroscopy with spectral acquisition from 250 to 600 nm using a 1:1 mole ratio (**AuL**:GSH) of the two reactants and is presented in Figure 5. The change in the spectrum of **AuL** observed was the appearance of two isosbestic points at 315 and 439 nm, respectively. The highest-energy band at 258 nm redshifts by only 3 nm to 261 nm, while the 354 nm band only redshifts by 2 nm to 356 nm. Inspection of the region around 354 nm indicates that two separate isosbestic points are established close to one another over the time course of the reaction, suggesting a biphasic reaction overall. The UV-vis spectra for the reaction of **AuL** with GSH reveal that the Au(III) metal ion is not reduced (i.e., from Au(III) to Au(I)/Au(0)). Instead, the formation of the isosbestic points and minor redshifted wavelengths are likely due to the binding of GSH to **AuL**, forming an **AuL**{GSH} adduct. The main reaction of GSH with **AuL** is described in eq. 3.

$$AuL + GSH \rightleftharpoons AuL-GSH + Cl^- \quad (3)$$

The kinetic trace of **AuL** in the presence of GSH was recorded from the time-dependent spectra at 258 nm and confirms the

Chem. Eur. J. **2025**, *31*, e202404345 (5 of 13)

© 2025 The Author(s). Chemistry – A European Journal published by Wiley-VCH GmbH

Chemistry–A European Journal

Research Article
doi.org/10.1002/chem.202404345

Chemistry
Europe
European Chemical
Societies Publishing

biphasic nature of the reaction with two distinct rate constants: $k_1 = 0.100(0.005)$ s^{-1} and $k_2 = 0.079(0.005)$ s^{-1}. The mean lifetimes for these steps are $\tau_1 = 42.61(4.4)$ s and $\tau_2 = 388.9(27)$ s. A comprehensive kinetic study of the reaction mechanism would be valuable and feasible for future work, although it is beyond the scope of the current article. Of particular significance is the observation that GSH does not reductively demetallate **AuL**; instead, a spectroscopically distinct Au^{III}-GSH adduct is formed and remains stable in the presence of excess GSH. Given that many Au^{III} complexes are reduced by GSH in vivo to either Au^{I} species or even completely to Au(0),[64] this study emphasizes the exceptional stability of Au^{III} conferred by the NNN pincer ligands.

2.2.4. Cytotoxicity of AuL in vitro

Following confirmation that **AuL** is sufficiently stable at physiological pH, we proceeded to assess its cytotoxicity in vitro. This was tested against two invasive adenocarcinoma cell lines namely MCF-7 (hormone responsive breast cancer) and HT-29 (colorectal cancer). Cell viability was investigated using an MTT (3-(4,5-dimethylthiazol-2-yl)-2,5-diphenyltetrazolium bromide) assay and early stages of apoptosis were detected using an APOPercentage assay. This section validates the effectiveness of **AuL** as a potential anti-cancer agent. 40 μM Plumbagin (PL) was utilized as a positive control for cell death. Plumbagin was used as the positive control in the MTT experiment because it is a well-characterized cytotoxic agent with a rapid and strong effect on cell viability, ensuring the assay's technical reliability. It exhibits broad-spectrum cytotoxicity and is commonly used in in vitro cytotoxicity studies. Unlike Auranofin or Cisplatin, Plumbagin exerts cytotoxic effects by inducing reactive oxygen species (ROS), triggering cell cycle arrest and apoptosis cell death primarily through ROS generation, providing a distinct mechanism from the test compound **AuL**. Plumbagin's consistent and broad-spectrum cytotoxicity makes it a widely accepted standard in in vitro assays.[65]

An MTT assay assesses the effect of a drug or compound on the cytotoxicity of cells, by measuring changes in cell viability.[66,67] Both cancer cell lines were exposed to a range of **AuL** concentrations (0–100 μM), over a period of 24 and 48 hours. **AuL** did not appear to have a cytotoxic effect in the HT-29 and MCF-7 cell line after 24 hours (Figure 6a). This is likely due to the slow uptake of **AuL** by the cells. Following 48 hours of exposure, there was not a significant reduction in cell viability in the HT-29 cells, in both the low (0.1-5 μM) and high (10-100 μM) concentration ranges, where IC$_{50}$ >100 μM, compared to the negative control (Figures 6b and c). Low toxicity of **AuL** in the HT-29 cells was confirmed with the APOPercentage assay. The red APOPercentage dye is selectively taken up by apoptotic cells, during the membrane flip of phosphatidylserine in the early stages of apoptosis.[68,69] Subsequently, cytotoxicity can be detected at 550 nm and visualized via microscopy. The micrographs indicate APOPercentage dye uptake following 48 hours exposure to **AuL** (Figure 6).

AuL did not induce significant apoptosis in both the low (5 μM) and high (100 μM) concentration range, at 6.3% and 8.3%, respectively, relative to the untreated control (Figure 6e). In the MCF-7 cell line, **AuL** was not shown to be cytotoxic in the low concentration range at 48 hours. However, at high concentrations, viability was significantly reduced, showing an IC$_{50}$ = 9 μM (Figures 6b and c). This IC$_{50}$ is comparable to that of cisplatin which has been recorded in literature to be within the range of 0.5 – 10 μM.[70–72] This shows that the cytotoxicity of **AuL** is comparable to cisplatin in breast cancer cells in vitro. Our data indicate that **AuL** could potentially be an effective anti-cancer agent in breast cancer.

This was validated following analysis of apoptosis. The apoptosis-inducing properties of **AuL** in MCF-7 cells was visualized at low concentrations of 5 and 10 μM (Figure 6f). **AuL** induced 33.9% and a significant 54.8% apoptosis in MCF-7 cells, at 5 and 10 μM (Figure 6g), which is comparable to the cell viability data. The sensitivity of **AuL** in MCF-7 cells and not in HT-29 cells indicates that this compound may act as an anti-cancer agent in selective cancer types, likely targeting breast cancer (oestrogen receptor positive, progesterone receptor positive). Further analysis is required to understand solution stability under physiological conditions, cellular uptake, and the mechanism of action of **AuL** in vitro.

Although direct comparison is not possible due to various variables, such as different incubation times, methodology for the cytotoxicity assay, and cell lines, our limited data for **AuL** compare favourably with the cytotoxicity reported for other gold(III) complexes, of which IC$_{50}$ values range from 0.1 to 35 μM against several different cell lines.[73–79] Importantly, **AuL** IC$_{50}$ values compared favourably to the closest set of Au^{III} pincer ligands we could find, IC$_{50}$ = 20 μM, for a class of [Au(N–N'–N)Cl]Cl$_2$[77] pincer complexes.

In contrast to the notable cytotoxicity of **AuL** against the MCF-7 cells, **H$_2$L** exhibited no significant cytotoxicity against either the MCF-7 or HT-9 cell lines at concentration below 100 μM

(Figure S15). These findings emphasize that the gold(III) ion, and its unique chemical properties, are essential for the efficacy of the gold(III) complex synthesized in this study. These collective findings are highly encouraging, as they demonstrate that the gold(III) chelates successfully reach their cellular targets before reduction or decomposition. Furthermore, the results highlight the critical role of the gold(III) ion in the efficacy of gold(III) chelates as chemotherapeutic agents, currently in vitro and potentially also in vivo going forward.

2.2.5. MOA of AuL with ctDNA–spectroscopic titrations

Based on the design of **AuL** and reported literature of gold(III) pincer complexes binding to DNA,[77] we investigated if **AuL** binding to DNA is a potential mechanism of action (MOA) of its cytotoxicity. The interaction between **AuL** and calf thymus deoxyribonucleic acid (ctDNA) was investigated by spectroscopic titrations (Figure 7), which indicates the change in the electronic spectrum of **AuL** for a single titration (of triplicate results). In Figure 7a, the red spectral line (before adding ctDNA to **AuL**) and the blue spectral line (after adding 37 μM of ctDNA) marks the end point, which is reached due to partial precipitation and
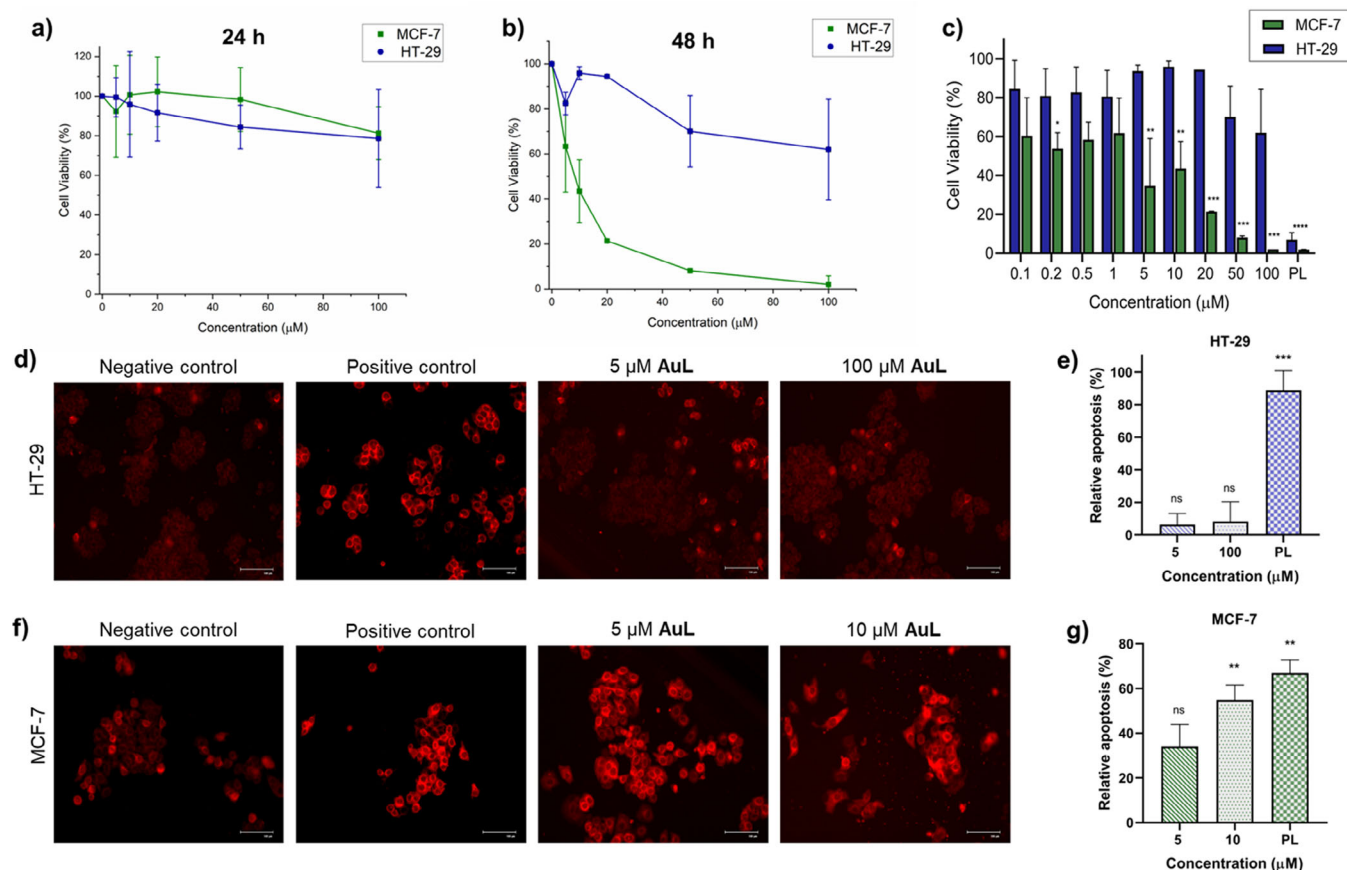
Chemistry–A European Journal

Research Article
doi.org/10.1002/chem.202404345

**Chemistry
Europe**
European Chemical
Societies Publishing

Figure 6. Cytotoxic effect of **AuL** in HT-29 and MCF-7 cells. Dose-response curves of **AuL** at **a)** 24 and **b)** 48 hours in HT-29 and MCF-7 cells. **c)** HT-29 and MCF-7 cell viability following exposure to 0.1, 0.2, 0.5, 1, 5, 10, 20, 50, and 100 μM **AuL**. 40 μM plumbagin (PL) acted as the positive control. Visual representation of the effect of **AuL** on apoptosis in **d)** HT-29 and **e)** MCF-7 cells. **f)** 5 μM and 100 μM **AuL** had no significant effect on HT-29 apoptosis, relative to the untreated group. **g)** 5 μM and 10 μM **AuL** induced 33.9% and 54.8% apoptosis in MCF-7 cells, relative to the untreated group. The scale bar represents 100 μm. Data represent the mean ± standard deviation. A one-way ANOVA was performed for statistical analysis, with Bonferroni's multiple comparisons test used for pairwise analyses, where * $P < 0.05$, ** $P < 0.01$, *** $P < 0.001$.

turbidity of the solutions after incremental additions of ctDNA. The electronic spectra (Figure 7a) indicate a nonlinear decrease in absorbance as a function of increasing ctDNA concentrations.

The hypochromic spectral changes of **AuL** were monitored at 342 nm (Figure 7b) and the nonlinear data set was fitted to the modified Hill-Langmuir model,[80,81] with a sigmoidal function using OriginPro2023.[60] This fit quantified the affinity of **AuL** to DNA as binding constants $K_{a1} = 1.48 \times 10^9$ M^{-1} and $K_{a2} = 6.59 \times 10^5$ with an R^2 value of 0.997, which indicated a relatively good fit (Figure 7b, Table 1). Furthermore, the 342 nm band exhibited minor bathochromic shifts in peak position (~2 nm), while isosbestic points were only observable at concentrations of ctDNA below 90 nM (insert in Figure 6a).

This hypochromicity is typical of most NNN type gold(III) pincer complexes in literature, however, the K_a values are several orders of magnitude greater than reported binding constants of other known gold(III) terpyridines 10^3 –10^5 M^{-1}.[77,82–86]

Interestingly, the resultant spectral profile of the interaction of **AuL** with ctDNA was partially similar to that of a cationic Ru(II)polypyridine complex (order of binding constant of 10^6)[87] and an anionic DNA-binding probe (order of binding constant of

10^2, where the low value was ascribed to the negative charge),[88] as they all exhibit a significant drop in absorbance between 300 –and 500 nm.

The DNA binding constants may be suggestive of the mode of binding of **AuL** to DNA. Alkylators typically exhibit moderately high binding constants, as they bind to DNA primarily through covalent bonding, with this interaction often being irreversible. In contrast, other types of DNA binding mainly depend on electrostatic, hydrophobic interactions, and π-π stacking (intercalation).[84,89,90] Notably, groove binders tend to have even higher binding constants, as they interact more deeply within the DNA grooves facilitating stronger and more stable binding.[91,92]

Most intercalators in the literature have binding constants between 10^3 –and 10^6 M^{-1}, examples of which include ethidium bromide (2.5 × 10^6 – 8.2 × 10^4 M^{-1})[93] psoralen (9.75 × 10^3 M^{-1}),[94] and acridine (1.74 × 10^4 – 1.0 × 10^6 M^{-1}).[95] Groove binders however generally have higher affinities with binding constants between 10^5 and 10^8 M^{-1}.[91,92] It is difficult to distinguish alkylators based on the binding constant, but some base-binding gold(III) pincer complexes have been reported to
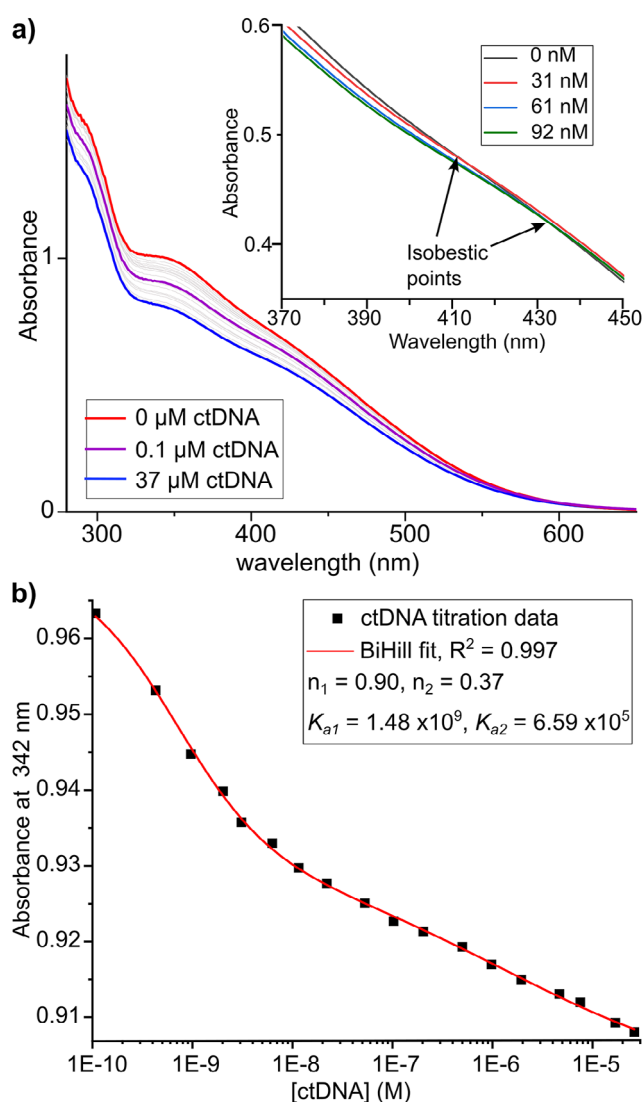
Chem. Eur. J. **2025**, *31*, e202404345 (7 of 13)

© 2025 The Author(s). Chemistry – A European Journal published by Wiley-VCH GmbH

Chemistry–A European Journal

Research Article
doi.org/10.1002/chem.202404345

Chemistry Europe
European Chemical
Societies Publishing

Figure 7. a) A representative of the triplicates for the UV-vis absorption spectra of 117 µM **AuL** in 0.10 M TRIS-HCl buffer 10% DMSO (red spectrum) after sequential additions of ctDNA from 0 to 0.1 µM (purple spectrum) and to a final concentration of 37 µM ctDNA before precipitation (blue spectrum). The insert shows the isosbestic points at low concentrations of DNA. b) Illustration of the UV-vis titration spectra monitored at 342 nm as a function of the concentration ctDNA at fixed **AuL** concentration.

Table 1. The binding parameters of DNA and its components with ctDNA.

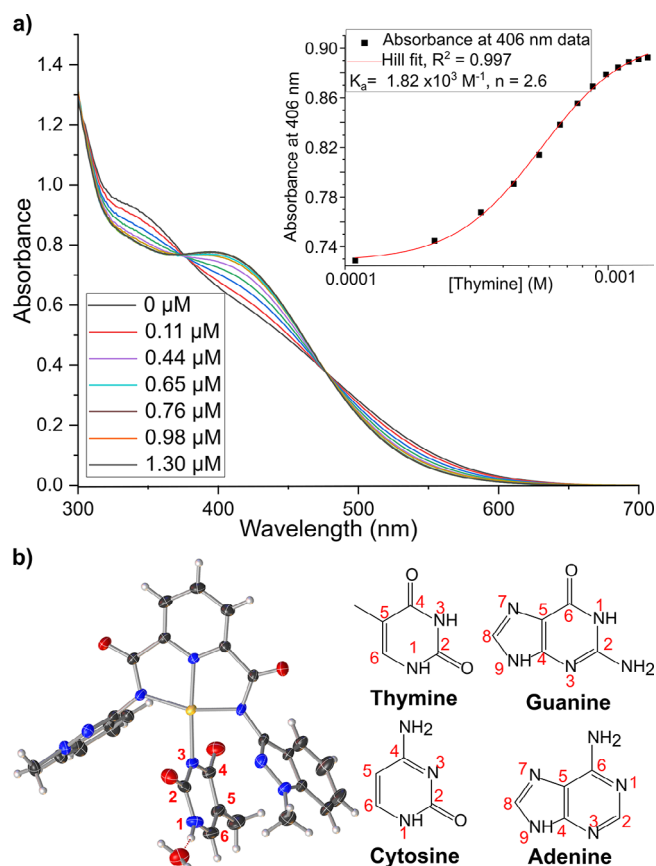| DNA		Binding constant [K_a] / M^{-1}	
	K_{a1}	$1.48. \times 10^9$	
	K_{a2}	$6.59. \times 10^5$	
	Base	Nucleoside	Nucleotide
Adenine	$1.21. \times 10^4$	$1.75. \times 10^3$	$3.72. \times 10^3$
Thymine	$1.83. \times 10^3$	$2.19. \times 10^3$	NA
Cytosine	$2.20. \times 10^3$	$1.74. \times 10^3$	$3.60. \times 10^3$
Guanine	NA	$1.65. \times 10^3$	$1.26. \times 10^3$
NA refers to the component not being available for testing.			

Figure 8. a) A representative of the titration triplicates for the UV-vis absorption spectra of 117 µM **AuL** in 0.10 M TRIS-HCl buffer 10% DMSO after sequential additions of thymine until the final concentration before precipitation. The insert graph illustrates the UV-vis titration spectra at 406 nm as a function of the increasing ratio (concentration) of thymine to **AuL**. b) An illustration showing the atom numbering on the thymine residue in **AuLT** along with the numbering of the DNA bases: guanine (G), adenine (A), cytosine (C), and thymine (T). The bases are linked to ribose through N1 for pyrimidines and N9 purines.

have binding constants of 4.5×10^5 and 5.4×10^5 M^{-1}. Although these ranges often overlap, they provide an insight on the binding mechanism of the binders.

The potential of **AuL** base-binding to ctDNA was investigated by electronic spectroscopy titration between the metal complex and DNA bases, nucleosides, and nucleotides (Figure 8a). This was done to delineate the binding behaviour of **AuL** with DNA components, and ATP, and to evaluate the impact of steric bulk (from ribose and phosphate groups) on **AuL**'s binding to DNA bases, as well as identify atoms involved in the base-binding of **AuL**.

The interaction between **AuL** and thymine (Figure 8), as well as other DNA components, was investigated through spectroscopic titrations within the 300–700 nm range. Hypochromic spectral changes of **AuL** were monitored between 400 and 450 nm for the various DNA components, and the nonlinear data were fitted to the Hill model (Figures 8 and S7 -S9).[80,81] This analysis quantified the affinity of **AuL** for the native DNA bases yielding K_a values ranging from 1.26×10^3 to 1.21×10^4 M^{-1} (Table 1). Unlike the titrations with ctDNA, minor bathochromic

Chem. Eur. J. **2025**, *31*, e202404345 (8 of 13)

© 2025 The Author(s). Chemistry – A European Journal published by Wiley-VCH GmbH

Chemistry–A European Journal

Research Article
doi.org/10.1002/chem.202404345

Chemistry
Europe
European Chemical
Societies Publishing

shifts (∼4 nm) were observed along with distinct isosbestic points throughout the titration with all bases, nucleosides and nucleotides, suggesting a permanent interaction (covalent bonding) between **AuL** and the DNA components.

The moderate binding affinities of the DNA components to **AuL** indicate that the gold(III) complex has the ability to interact directly with these DNA residues. Notably, we successfully obtained a crystal structure of the **AuL** complex with thymine (**AuLT**; Figures 2b and 8b). Despite many attempts with all four native DNA bases, only the complex with thymine was successfully crystallized.

The binding of **AuL** with thymine in Figures 2b and 8b shows a preference for the N3 position over N1, likely due to the polarized N3-H bond. This polarization facilitates deprotonation, and making N3 more reactive than N1.[96] Studies indicate that alkylating agents like cisplatin preferentially bind at the N7 position in guanine, suggesting that N1 in pyrimidines and N9 in purines are not central to alkylation.[97] Consequently, it is proposed that **AuL**, as a "DNA alkylator", will similarly favor binding at N3 in pyrimidines and N7 in purines. The N7 position in purines is more accessible, as it is not involved in hydrogen bonding between bases or in the base-sugar linkage, which may explain the binding preference of metal complexes like cisplatin for guanine.[98] Conversely, the involvement of N3 in purines in hydrogen bonding with adenine in double helix DNA limits its availability for metal complex binding, unless conformational displacement of thymine from the base stack occurs during the reaction.

Our data for the titration of **AuL** with the four native DNA components (base, nucleoside, nucleotide) suggest that the interactions involve the same donor atom across these targets, and presumably also double-stranded DNA. Notably, the increase in molecular size from bases to nucleotides did not significantly impact the binding affinity of A, C, G, and T components to **AuL** (Table 1). While smaller DNA components might be expected to bind more efficiently to **AuL** than the full DNA structure, steric hindrance did not substantially affect binding among bases, nucleosides, and nucleotides. This observation suggests that steric bulk from ribose and phosphate groups does not obstruct the complexation process. Rather, electronic factors appear to predominantly govern the reactivity of these components.

Adenine exhibited a relatively higher binding affinity to **AuL** compared to guanine, cytosine, and thymine, though no consistent trend was observed among nucleotides and nucleosides, indicating no clear preference. The binding constants for bases, nucleosides, and nucleotides were moderately high, ranging from 1.26×10^3 to 1.21×10^4 M^{-1}, suggesting that alkylation may be a primary interaction mode for **AuL** with DNA.

2.3. Linear dichroism (LD) and circular dichroism (CD) of DNA

The linear dichroism (LD) spectra of ctDNA and ctDNA with **AuL** (ctDNA-**AuL**) are depicted in Figure 9a, while ctDNA with Hoechst 33 258 (ctDNA-hoechst stain [HS]) and with ethidium bromide (ctDNA-ethidium bromide [EB]) served as comparison controls (Figure S10c). The ctDNA-**AuL** system has a negative sig-
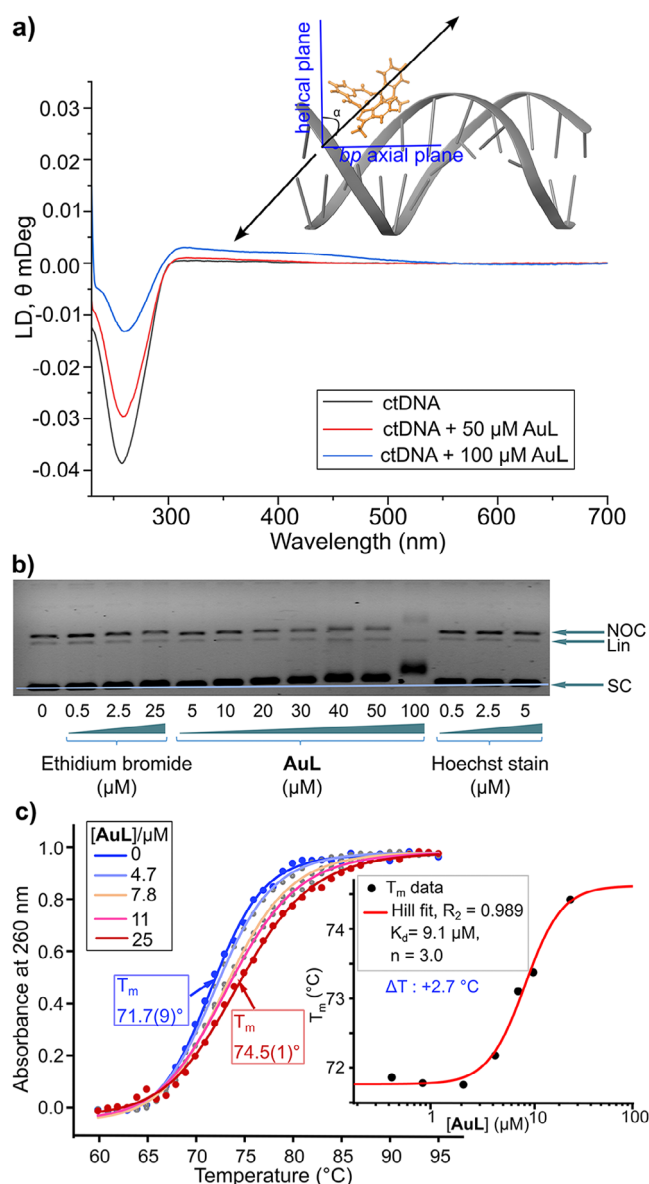

Figure 9. a) The LD spectrum of **AuL** with 100 μM of ctDNA at increasing **AuL** concentration in KH$_2$PO$_4$ (50 mM, pH 7.5) at 37 °C. The intense minimum at 260 nm represents ctDNA and the 300–540 nm band represents an induced gold(III) complex LD spectrum. b) EMSA agarose gel for **AuL** with pUC57 (2.5 ng/well, 1x TAE buffer, 5% v/v DMSO). The DNA bands formed are for supercoiled (SC), nicked-open circular (NOC), and linear (Lin). Lane 1 is the control lane containing ctDNA only. Lanes 2–14 have increasing concentrations of **EB** (2–4), **AuL** (5–11), and Hoechst 33 258 (**HS**, 12–14), and they compare the behaviour of a DNA intercalator, **EB**, the gold(III) complex, and a DNA minor groove binder, **HS** respectively. Experiments were done in triplicates and a representative assay is shown. c) The melt curves for ctDNA with different concentrations of **AuL** to calculate T$_m$ from the Boltzmann sigmoidal fit. The inset is the change in T$_m$ with the change in [**AuL**], fitted to a Hill sigmoidal function (T$_m$ = +2.7 °C).

nal throughout the π−π* region of the LD spectra (230–290 nm), with a minimum at 260 nm, as a result of the nitrogenous bases within ctDNA.[99] This is indicative that the transition moments are oriented perpendicular to the helix axis. Figure 9a highlights that the 260 nm minimum decreases in a dose-dependent manner (i.e., with increasing **AuL** concentration). This is due to **AuL**

Chem. Eur. J. **2025**, *31*, e202404345 (9 of 13)

© 2025 The Author(s). Chemistry – A European Journal published by Wiley-VCH GmbH

Chemistry–A European Journal

Research Article
doi.org/10.1002/chem.202404345

Chemistry
Europe
European Chemical
Societies Publishing

binding within the nucleobases of ctDNA, suggesting that its ability to orient along the perpendicular flow lines is significantly impaired as function of **AuL** concentration. The observation that the induced LD signal from the $\pi-\pi^*$ bands of **AuL** ($\sim$400 nm) becomes increasingly positive in the LD spectrum at higher [**AuL**] is consistent with the spectroscopic signature of ctDNA-HS, a known minor groove binder Figure S10d.[100]

Regarding the induced dichroic signal observed between 300 and 540 nm, this is specifically in a spectral region where no contribution from the ctDNA nucleobases can be detected and only **AuL** absorbs. **AuL** itself is isotropic and cannot be orientated in the flow field. Therefore, the dichroic signal peaking is indicative of an induced LD signal[101] and its occurrence suggests that **AuL** forms a molecular complex with ctDNA, resulting in the bound complex becoming oriented in the flow field. The positive dichroic signal signifies that the $\pi-\pi^*$ transition dipoles of **AuL** are in a plane tilted almost 45° in relation to the helix axis, consistent with minor groove binders. Furthermore, the data are consistent with that of HS binding to ctDNA; a strong positive induced LD signal was observed with a maximum at 347 nm (Figure S10). This is consistent with previously reported induced LD spectra of HS.[102] From Figure S10d, we see HS is orientated close to 45° to the base pair plane and helical axis, indicating it is a grove binder.[91]

2.3.1. Electrophoresis

To corroborate the data from LD spectroscopy, we conducted electrophoretic mobility shift assays (EMSA)[103] to examine alterations in the tertiary and secondary structure of pUC57 plasmid DNA. EMSA was performed using plasmid DNA equilibrated with varying concentrations of **AuL**, **HS**, and **EB**. As shown in Figure 9b, the reference lane contained only native DNA, representing the mobility of untreated pUC57 plasmid DNA. **EB** served as an intercalator control, while **HS** acted as a control for a minor groove binder. The well-defined binding modes of both **EB** and **HS** to pUC57 plasmid DNA made them suitable controls, with their migration patterns in the EMSA gel helping to evaluate the binding mode of **AuL** to pUC57 plasmid DNA.

In the EMSA gel, linear pUC57 plasmid DNA is marginally affected by the binding of either the intercalator or the minor groove binder. The binding of **EB** reduces the mobility of supercoiled (SC) and nicked-open circular (NOC) pUC57 plasmid DNA on the agarose gel.[104] This reduction occurs because intercalation partially unwinds the SC DNA, increasing steric bulkiness in the NOC form, thereby reducing mobility due to increased hydrodynamic drag.[104] Conversely, the minor groove binder **HS** increases DNA mobility along the gel, as the DNA molecules become more compactly packed.[91] Although the change is less pronounced than with **EB**, an increase in **HS** concentration enhances the supercoiling of SC DNA, resulting in increased mobility across the agarose gel. As shown in Figure 8b, **EB** binding reduces DNA mobility in a concentration-dependent manner, whereas **HS** exhibits the opposite effect.

The **AuL** complex exhibited a pronounced reduction in the mobility of SC and NOC pUC57 plasmid DNA, suggesting a strong interaction between **AuL** and pUC57 plasmid DNA, and

likely involving alkylation. When **AuL** covalently binds to the DNA bases (alkylation), it increases the bulkiness of the pUC57 plasmid DNA, causing kinking and resulting in higher hydrodynamic drag and reduced mobility on the gel. This reduction in pUC57 plasmid DNA mobility is apparent even at low concentrations, starting from 10 μM, highlighting **AuL** as a DNA alkylator. This is consistent with findings in literature where cisplatin, a prototypical alkylating agent, exhibits comparably high hydrodynamic drag due to its interaction with DNA and its subsequent structural modifications.[105–108] To reinforce these EMSA findings, additional experiments were conducted.

2.3.2. Thermal melt analysis

The thermal melt temperature (T_m) of ctDNA was analysed in the presence of **AuL** to elucidate the two potential binding mechanisms of the complex to DNA (Figure 9c). At the highest concentration of **AuL** (25 μM), the observed ΔT_m was +2.7 °C. While DNA intercalators typically increase the T_m by at least 5 °C, minor groove binders tend to slightly increase the T_m (<5 °C).[109] Minor groove binders stabilize the DNA double helix structure through hydrogen bonding and van der Waals interaction within the groove, which enhances the overall structural integrity of the DNA.[110–112] Conversely, alkylators disrupt base pair interactions, leading to local denaturing, and a decrease in T_m of ctDNA.[113–115] This effect is characteristic of monofunctional alkylation, while bifunctional alkylation (interstrand crosslinking) stabilizes the DNA, thereby increasing the energy required for denaturation and elevating T_m.

As shown in Figure 9c, at **AuL**:ctDNA concentration ratios of below 0.05, a slight decrease in the T_m was observed, indicative of alkylation. At higher ratios (above 0.05), the data suggest that minor groove binding also contributes to the observed interactions.

The modest ΔT_m of +2.7 °C, along with the two binding constants (K_{a1} and K_{a2}) and the LD and EMSA data, supports a mechanism involving dual binding modes of **AuL** to DNA: specifically, minor groove binding and alkylation. This conclusion is further substantiated by viscosity data Figure S11.

2.3.3. Biomolecular simulations

To further corroborate the binding mechanism of **AuL** to DNA, we incorporated molecular dynamics (MD) simulations. This was achieved by first docking **AuL** into two oligonucleotides using Glide XP. The two DNA oligonucleotide X-ray structures used were PDB 425D (2.80 Å)[116] and PDB 4E1U (0.92 Å)[117] for flexible ligand docking. Docking data are presented in Figure S12. MD simulations may aid in drawing conclusions based on the interactions between the oligonucleotide and **AuL** over the simulated time, capturing the system's dynamic behaviour and offering a more accurate reflection of physiological conditions.[118] As shown in Figure 10, the root-mean-square deviation (RMSD) of **AuL** indicates that it remains stably bound within the minor grove of an AT cluster until 79 ns, thereafter a large deviation is observed for about 2 ns before an equilibrium is reached, with **AuL** now occupying a new conformation within DNA. The
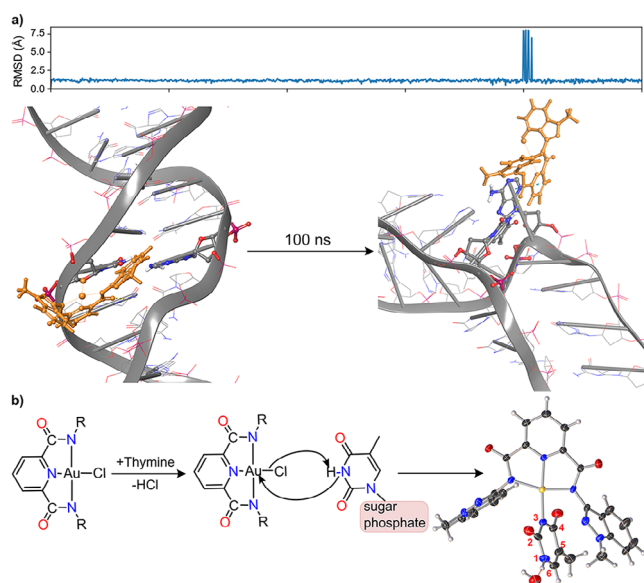
Chem. Eur. J. 2025, *31*, e202404345 (10 of 13)

© 2025 The Author(s). Chemistry – A European Journal published by Wiley-VCH GmbH

Chemistry–A European Journal

Research Article
doi.org/10.1002/chem.202404345

Chemistry Europe
European Chemical
Societies Publishing

Figure 10. a) Molecular dynamics (MD) simulation over 100 ns of the best-docked GLIDE XP structure of **AuL** binding within the minor groove of a DNA oligonucleotide (PDB 425D[116], 5′-D(ACCGACGTCGGT)-3′; ligand removed). A large target grid was generated for ligand docking at nucleic acid sites close to the centre of the DNA (with all solvents removed), spanning $40 \times 40 \times 40$ Å³, thereby facilitating a search of alternative binding pockets radiating throughout the oligonucleotide. The RMSD indicates that there is minimal fluctuation of complex **AuL** throughout the MD trajectory. b) Proposed reaction mechanism of **AuL** binding to an AT cluster and alkylating via N3 on the thymine residue.

MD simulation to a degree corroborates the experimental data (*vide supra*), indicating a dual binding mechanism: (i) initially minor groove binding and (ii) alkylation. Due to the limitations of Desmond with regards to metal complexes, alkylation would not be accurately portrayed.

Based on comprehensive experimental and theoretical data, we propose a probable mechanism by which **AuL** interacts with DNA (Figure 10b). Initially, **AuL** binds to the minor groove of DNA, specifically within an AT-rich cluster, with an affinity constant (K_a) of 1.48×10^9 M⁻¹, which is consistent with typical values for groove binders. Following this, a second binding event occurs wherein the coordinated chloride ion is displaced by the amide of a thymine residue through nucleophilic substitution. This secondary interaction, referred to as alkylation, proceeds with an affinity constant of 6.59×10^5 M⁻¹.

3. Conclusion

A cytotoxic indazole-based gold(III) complex, **AuL**, was successfully synthesized. **AuL** demonstrated significant cytotoxicity against the MCF-7 breast cancer cell line, with activity comparable to that of cisplatin, despite showing limited effects against the HT-29 colon cancer cell line. The interaction of **AuL** with DNA was investigated using various biophysical techniques, which revealed dual binding modes: at lower concentrations, **AuL** predominantly binds within the minor groove, while at higher concentrations, alkylation (covalent binding) becomes signifi-

cant. Biomolecular simulations further supported minor groove binding; however, confirmation of alkylation was limited by the constraints of the Desmond software.

A proposed interaction scheme suggests that **AuL** initially binds to the minor groove of the DNA double helix, followed by interactions with DNA bases as concentration increases. This dual binding mechanism highlights the potential of **AuL** as an effective anticancer agent, warranting further investigation. Importantly, the dual binding behaviour of **AuL** suggests broader implications for drug design, particularly in developing novel metal-based therapeutics that can target DNA through multiple modes of interaction. While the interaction of the complex with DNA may play a crucial role in its cytotoxicity, it remains unclear whether this is the primary in vitro cellular target as studies to confirm this are still ongoing. Additional pathways, including potential interactions with cellular proteins, remain to be explored, opening avenues for future studies and optimization in therapeutic applications.

Supporting Information

Crystallographic data: Deposition numbers 2403562 and 2403563 contain the supplementary crystallographic data for this paper. These data are provided free of charge by the joint Cambridge Crystallographic Data Centre and Fachinformationszentrum Karlsruhe Access Structures service.

Acknowledgments

Conflict of Interest

The authors declare no conflict of interest.

Data Availability Statement

The data that support the findings of this study are available on request from the corresponding author. The data are not publicly available due to privacy or ethical restrictions.

Chem. Eur. J. **2025**, *31*, e202404345 (11 of 13)

© 2025 The Author(s). Chemistry – A European Journal published by Wiley-VCH GmbH

[1] C. Roder, M. J. Thomson, *Drugs R D* **2015**, *15*, 13.

[2] P. Calamai, S. Carotti, A. Guerri, T. Mazzei, L. Messori, E. Mini, P. Orioli, G. P. Speroni, *Anti-cancer drug design* **1998**, *13*, 67.

[3] C.-M. Che, R. W.-Y. Sun, W.-Y. Yu, C.-B. Ko, N. Zhu, H. Sun, *Chem. Commun.* **2003**, 1718.

[4] Y. Lu, X. Ma, X. Chang, Z. Liang, L. Lv, M. Shan, Q. Lu, Z. Wen, R. Gust, W. Liu, *Chem. Soc. Rev.* **2022**, *51*, 5518.

[5] Y. Sun, Y. Lu, M. Bian, Z. Yang, X. Ma, W. Liu, *Eur. J. Med. Chem.* **2021**, *211*, 113098.

[6] M. Bian, X. Wang, Y. Sun, W. Liu, *Eur. J. Med. Chem.* **2020**, *193*, 112234.

[7] G. Sági, K. Szűcs, G. Vereb, L. Otvös, *J. Med. Chem.* **1992**, *35*, 4549.

[8] S. Mal, U. Malik, M. Mahapatra, A. Mishra, D. Pal, S. K. Paidesetty, *Drug Dev. Res.* **2022**, *83*, 1469.

[9] N. A. S. Ali, B. A. Dar, V. Pradhan, M. Farooqui, *Mini Rev Med Chem* **2013**, *13*, 1792.

[10] L. Mosti, G. Menozzi, P. Fossa, W. Filippelli, S. Gessi, B. Rinaldi, G. Falcone, *Arzneimittelforschung* **2000**, *50*, 963.

[11] V. K. Tandon, D. B. Yadav, A. K. Chaturvedi, P. K. Shukla, *Bioorg. Med. Chem. Lett.* **2005**, *15*, 3288.

[12] D. Raffa, G. Daidone, B. Maggio, D. Schillaci, F. Plescia, *Archiv der Pharmazie* **1999**, *332*, 317.

[13] J.-H. Sun, C. A. Teleha, J.-S. Yan, J. D. Rodgers, D. A. Nugiel, *J. Org. Chem.* **1997**, *62*, 5627.

[14] M. Patel, R. F. Kaltenbach, D. A. Nugiel, R. J. McHugh, P. K. Jadhav, L. T. Bacheler, B. C. Cordova, R. M. Klabe, S. Erickson-Viitanen, S. Garber, C. Reid, S. P. Seitz, *Bioorg. Med. Chem. Lett.* **1998**, *8*, 1077.

[15] W. Han, J. C. Pelletier, C. N. Hodge, *Bioorg. Med. Chem. Lett.* **1998**, *8*, 3615.

[16] M. Boulouard, P. Schumann-Bard, S. Butt-Gueulle, E. Lohou, S. Stiebing, V. Collot, S. Rault, *Bioorg. Med. Chem. Lett.* **2007**, *17*, 3177.

[17] V. J. Arán, C. Ochoa, L. Boiani, P. Buccino, H. Cerecetto, A. Gerpe, M. González, D. Montero, J. J. Nogal, A. Gómez-Barrio, A. Azqueta, A. López de Ceráin, O. E. Piro, E. E. Castellano, *Bioorg. Med. Chem.* **2005**, *13*, 3197.

[18] J. D. Rodgers, B. L. Johnson, H. Wang, R. A. Greenberg, S. Erickson-Viitanen, R. M. Klabe, B. C. Cordova, M. M. Rayner, G. N. Lam, C.-H. Chang, *Bioorg. Med. Chem. Lett.* **1996**, *6*, 2919.

[19] S. Bräse, C. Gil, K. Knepper, *Bioorg. Med. Chem.* **2002**, *10*, 2415.

[20] M. K. Brawer, *Rev Urol* **2005**, *7*, S21.

[21] C. M. Carapella, M. G. Paggi, F. Calvosa, F. Cattani, B. Jandolo, R. Mastrostefano, L. Raus, A. Riccio, *J Neurosurg Sci* **1990**, *34*, 261.

[22] P. Feyer, M. H. Seegenschmiedt, M. Steingraeber, *Support Care Cancer* **2005**, *13*, 671.

[23] M. Tan, *Expert Opin Pharmacother* **2003**, *4*, 1563.

[24] T. J. Gan, *CNS Drugs* **2005**, *19*, 225.

[25] M. Gross-Goupil, L. François, A. Quivy, A. Ravaud, *Clin Med Insights Oncol* **2013**, *7*, 269.

[26] E. D. Deeks, *Drugs* **2012**, *72*, 2129.

[27] Y. Deng, C. Sychterz, A. B. Suttle, M. M. Dar, D. Bershas, K. Negash, Y. Qian, E. P. Chen, P. D. Gorycki, M. Y. K. Ho, *Xenobiotica* **2013**, *43*, 443.

[28] G. Sonpavde, T. E. Hutson, C. N. Sternberg, *Expert Opin Investig Drugs* **2008**, *17*, 253.

[29] J. Verweij, S. Sleijfer, *Expert Opin Pharmacother* **2013**, *14*, 929.

[30] Y.-A. Heo, S. T. Duggan, *Targ Oncol* **2018**, *13*, 533.

[31] G. Ison, L. J. Howie, L. Amiri-Kordestani, L. Zhang, S. Tang, R. Sridhara, V. Pierre, R. Charlab, A. Ramamoorthy, P. Song, F. Li, J. Yu, W. Manheng, T. R. Palmby, S. Ghosh, H. N. Horne, E. Y. Lee, R. Philip, K. Dave, X. H. Chen, S. L. Kelly, K. G. Janoria, A. Banerjee, O. Eradiri, J. Dinin, K. B. Goldberg, W. F. Pierce, A. Ibrahim, P. G. Kluetz, G. M. Blumenthal, J. A. Beaver, R. Pazdur, *Clin. Cancer Res.* **2018**, *24*, 4066.

[32] A. Chen, *Chin. J. Cancer.* **2011**, *30*, 463.

[33] H. Cerecetto, A. Gerpe, M. González, V. J. Arán, C. O. de Ocáriz, *Mini Rev Med Chem* **2005**, *5*, 869.

[34] M. A. Jakupec, E. Reisner, A. Eichinger, M. Pongratz, V. B. Arion, M. S. Galanski, C. G. Hartinger, B. K. Keppler, *J. Med. Chem.* **2005**, *48*, 2831.

[35] H. H. Showalter, M. M. Angelo, E. M. Berman, G. D. Kanter, D. F. Ortwine, S. G. Ross-Kesten, A. D. Sercel, W. R. Turner, L. M. Werbel, *J. Med. Chem.* **1988**, *31*, 1527.

[36] M. W. Johnson, A. G. DiPasquale, R. G. Bergman, F. D. Toste, *Organometallics* **2014**, *33*, 4169.

[37] W.-P. To, G. S.-M. Tong, W. Lu, C. Ma, J. Liu, A. L.-F. Chow, C.-M. Che, *Angew. Chem., Int. Ed.* **2012**, *51*, 2654.

[38] K. M.-C. Wong, L.-L. Hung, W. H. Lam, N. Zhu, V. W.-W. Yam, *J. Am. Chem. Soc.* **2007**, *129*, 4350.

[39] R. M. de Figueiredo, J.-S. Suppo, J.-M. Campagne, *Chem. Rev.* **2016**, *116*, 12029.

[40] V. R. Pattabiraman, J. W. Bode, *Nature* **2011**, *480*, 471.

[41] J. S. Carey, D. Laffan, C. Thomson, M. T. Williams, *Org. Biomol. Chem.* **2006**, *4*, 2337.

[42] K. T. Neumann, A. S. Donslund, T. L. Andersen, D. U. Nielsen, T. Skrydstrup, *Chem. Eur. J.* **2018**, *24*, 14946.

[43] R. M. Lanigan, T. D. Sheppard, *Eur. J. Org. Chem.* **2013**, *2013*, 7453.

[44] B. Alberts, A. Johnson, J. Lewis, M. Raff, K. Roberts, P. Walter, in *Molecular Biology of the Cell* 4th ed., Garland Science.

[45] K. Collins, T. Jacks, N. P. Pavletich, *Proc. Natl. Acad. Sci. USA* **1997**, *94*, 2776.

[46] G. M. Cooper, R. E. Hausman, *The Cell: A Molecular Approach*, ASM Press; Sinauer Associates, Washington, D.C. : Sunderland, Mass, **2007**.

[47] R. Razuwika, O. Q. Munro, *New J. Chem.* **2024**, *48*, 4229.

[48] N. S. Akhmadullina, A. V. Churakov, V. M. Retivov, R. A. Sandu, O. N. Shishilov, *Russ. J. Coord. Chem.* **2012**, *38*, 589.

[49] M. Hanif, S. Moon, M. P. Sullivan, S. Movassaghi, M. Kubanik, D. C. Goldstone, T. Söhnel, S. M. F. Jamieson, C. G. Hartinger, *J. Inorg. Biochem.* **2016**, *165*, 100.

[50] R. Graeser, R. Esser, H. Unger, I. Fichtner, A. Zhu, C. Unger, F. Kratz, *Invest New Drugs* **2010**, *28*, 14.

[51] W. H. Ang, E. Daldini, L. Juillerat-Jeanneret, P. J. Dyson, *Inorg. Chem.* **2007**, *46*, 9048.

[52] A. Casini, M. C. Diawara, R. Scopelliti, S. M. Zakeeruddin, M. Grätzel, P. J. Dyson, *Dalton Trans.* **2010**, *39*, 2239.

[53] V. Rousseau, H. G. Lindwall, *J. Am. Chem. Soc.* **1950**, *72*, 3047.

[54] A. Roniboss, K. Chanda, M. Motilal Balamurali, *ChemistrySelect* **2020**, *5*, 7505–7516.

[55] Y. Zhu, F. Liao, G. Suning, A. Gao, S. Lu, M. Shao, *J. Electrochem. Soc.* August 8, **2014**, *161*, B265.

[56] M. Sankar, R. G. Bates, *Anal. Chem.* **1978**, *50*, 1922.

[57] L. V. Salgado, C. Vargas-Hernández, *Am. J. Anal. Chem.* **2014**, *5*, 1290.

[58] T. M., "Buffers for the physiological pH range: acidic dissociation constants of zwitterionic compounds in various hydroorganic media," https://doi.org/10.1002/adic.200590001 can be found under https://pubmed.ncbi.nlm.nih.gov/15801182/, **2005**.

[59] N. Karimova, O. Alija, S. L. M. García, V. H. Grassian, R. B. Gerber, J. G. Navea, *Phys. Chem. Chem. Phys.* **2023**, *25*, 17306.

[60] OriginLab Corporation, **n.d.**

[61] J. P. Richie, S. Nichenametla, W. Neidig, A. Calcagnotto, J. S. Haley, T. D. Schell, J. E. Muscat, *Eur. J. Nutr.* **2015**, *54*, 251.

[62] "Reduced Glutathione | Pure | Doctors and Patients Access," can be found under https://www.pureencapsulationspro.com/reduced-glutathione.html, **n.d.**

[63] A. Krezel, W. Bal, *Acta Biochim. Pol.* **1999**, *46*, 567.

[64] T. Zou, C. T. Lum, C.-N. Lok, J.-J. Zhang, C.-M. Che, *Chem. Soc. Rev.* **2015**, *44*, 8786.

[65] S. Sagar, L. Esau, B. Moosa, N. M. Khashab, V. B. Bajic, M. Kaur, *Anticancer Agents Med Chem.* **2014**, *14*, 170.

[66] M. V. Berridge, P. M. Herst, A. S. Tan, in *Biotechnology Annual Review*. Elsevier, **2005**, pp. 127.

[67] M. Ghasemi, T. Turnbull, S. Sebastian, I. Kempson, *Int. J. Mol. Sci.* **2021**, *22*, 12827.

[68] M. Oancea, S. Mazumder, M. E. Crosby, A. Almasan, *Methods Mol Med* **2006**, *129*, 279.

[69] O. Kepp, L. Galluzzi, M. Lipinski, J. Yuan, G. Kroemer, *Nat Rev Drug Discov* **2011**, *10*, 221.

[70] T. Kashkoulinejad-Kouhi, S. Safarian, B. Arnaiz, L. Saa, *Oncol Rep* **2021**, *45*, 665.

[71] J. Suberu, I. Romero-Canelón, N. Sulluvan, A. Lapkin, G. Barker, *ChemMedChem* **2014**, https://doi.org/10.1002/cmdc.201402285.

[72] J. Zou, L. Zhu, X. Jiang, Y. Wang, Y. Wang, X. Wang, B. Chen, *Oncotarget* **2018**, *9*, 11268.

[73] A. Casini, R. W.-Y. Sun, I. Ott, in *Metal Ions in Life Sciences* (Eds.: A. Sigel, H. Sigel, E. Freisinger, R.K.O. Sigel), De Gruyter, Berlin, Boston, **2018**, pp. 199.

[74] S. Sookai, M. P. Akerman, O. Q. Munro, *Dalton Trans.* **2024**, *53*, 5089.

[75] D. Van der Westhuizen, C. A. Slabber, M. A. Fernandes, D. F. Joubert, G. Kleinhans, C. J. van der Westhuizen, A. Stander, O. Q. Munro, D. I. Bezuidenhout, *Chemi. Eur. J.* **2021**, *27*, 8295.

[76] K. J. Akerman, A. M. Fagenson, V. Cyril, M. Taylor, M. T. Muller, M. P. Akerman, O. Q. Munro, *J. Am. Chem. Soc.* **2014**, *136*, 5670.

[77] S. Radisavljević, I. Bratsos, A. Scheurer, J. Korzekwa, R. Masnikosa, A. Tot, N. Gligorijević, S. Radulović, A. R. Simović, *Dalton Trans.* **2018**, *47*, 13696.

[78] B. Bertrand, M. A. O'Connell, Z. A. E. Waller, M. Bochmann, *Chem. Eur. J.* **2018**, *24*, 3613.

[79] S. Sookai, M. Akerman, M. Færch, Y. Sayed, O. Q. Munro, *Eur. J. Med. Chem.* **2025**, 117330.

[80] S. Goutelle, M. Maurin, F. Rougier, X. Barbaut, L. Bourguignon, M. Ducher, P. Maire, *Fundam. Clin. Pharmacol.* **2008**, *22*, 633.

[81] R. Gesztelyi, J. Zsuga, A. Kemeny-Beke, B. Varga, B. Juhasz, A. Tosaki, *Arch. Hist. Exact Sci.* **2012**, *66*, 427.

[82] "Pincer Compounds –1st Edition," can be found under https://www.elsevier.com/books/pincer-compounds/morales-morales/978-0-12-812931-9, n.d.

[83] J. J. Yan, A. L.-F. Chow, C.-H. Leung, R. W.-Y. Sun, D.-L. Ma, C.-M. Che, *Chem. Commun.* **2010**, *46*, 3893.

[84] D. van der Westhuizen, C. A. Slabber, M. A. Fernandes, D. F. Joubert, G. Kleinhans, C. J. van der Westhuizen, A. Stander, O. Q. Munro, D. I. Bezuidenhout, *Chem. Eur. J.* **2021**, *27*, 8295.

[85] B. Bertrand, M. R. M. Williams, M. Bochmann, *Chem.–Eur. J.* **2018**, *24*, 11840.

[86] S. Radisavljević, B. Petrović, *Front Chem* **2020**, *8*, 379.

[87] B. C. Poulsen, S. Estalayo-Adrián, S. Blasco, S. A. Bright, J. M. Kelly, D. C. Williams, T. Gunnlaugsson, *Dalton Trans.* **2016**, *45*, 18208.

[88] S. Ghosh, P. Kundu, B. K. Paul, N. Chattopadhyay, *RSC Adv.* **2014**, *4*, 63549–63558.

[89] S. Li, V. R. Cooper, T. Thonhauser, B. I. Lundqvist, D. C. Langreth, *J. Phys. Chem. B* **2009**, *113*, 11166.

[90] I. Ahmad, M. Ahmad, *Int. J. Biol. Macromol.* **2015**, *79*, 193.

[91] P. E. Pjura, K. Grzeskowiak, R. E. Dickerson, *J. Mol. Biol.* **1987**, *197*, 257.

[92] B. H. Geierstanger, D. E. Wemmer, *Annu. Rev. Biophys. Biomol. Struct.* **1995**, *24*, 463.

[93] J.-B. Lepecq, C. Paoletti, *J. Mol. Biol.* **1967**, *27*, 87.

[94] X. Zhou, G. Zhang, L. Wang, *Int. J. Biol. Macromol.* **2014**, *67*, 228.

[95] S. M. V. De Almeida, E. A. Lafayette, L. P. B. G. Da Silva, C. A. C. da Amorim, T. B. De Oliveira, A. L. T. G. Ruiz, J. E. De Carvalho, R. O. De Moura, E. I. C. Beltrão, M. D. C. A. De Lima, L. B. C. de Júnior, *Int. J. Mol. Sci.* **2015**, *16*, 13023–13042.

[96] S. Perreault, F. Arjmand, J. Chandrasekhar, J. Hao, K. S. Keegan, D. Koditek, E.-I. Lepist, C. K. Matson, M. E. McGrath, L. Patel, K. Sedillo, J. Therrien, N. A. Till, A. Tomkinson, J. Treiberg, Y. Zherebina, G. Phillips, *ACS Med. Chem. Lett.* **2020**, *11*, 1236.

[97] W. Zeng, Y. Zhang, W. Zheng, Q. Luo, J. Han, J. Liu, Y. Zhao, F. Jia, K. Wu, F. Wang, *Molecules* **2019**, *24*, 1852.

[98] S. Ghosh, *Bioorg. Chem.* **2019**, *88*, 102925.

[99] B. Nordén, T. Kurucsev, *J. Mol. Recognit.* **1994**, *7*, 141.

[100] B. Chazotte, *Cold Spring Harb Protoc* **2011**, *2011*, pdb.protpdb.prot5557.

[101] S. Sookai, M. L. Bracken, M. Nowakowska, *Molecules* **2023**, *28*, 7466.

[102] M. R. Hicks, J. Kowa\lski, A. Rodger, *Chem. Soc. Rev.* **2010**, *39*, 3380.

[103] H. R. Reese, *Biopolymers* **1994**, *34*, 1349.

[104] J. Sigmon, L. L. Larcom, *Electrophoresis* **1996**, *17*, 1524.

[105] B. Zhang, S. Seki, K. Akiyama, K. Tsutsui, T. Li, K. Nagao, *Acta Med. Okayama* **1992**, *46*, 427.

[106] S. Seki, A. Hongo, B. Zhang, K. Akiyama, A. H. Sarker, T. Kudo, *Jap. Jo. Cancer Res.* **1993**, *84*, 462–467.

[107] B. W. Johnson, M. W. Burgess, V. Murray, J. R. Aldrich-Wright, M. D. Temple, *BMC Cancer* **2018**, *18*, 1284.

[108] H. Atsushi, S. Shuji, A. Kosuke, K. Takafumi, *Int. J. Biochem.* **1994**, *26*, 1009.

[109] S. U. Rehman, T. Sarwar, M. A. Husain, H. M. Ishqi, M. Tabish, *Arch. Biochem. Biophys.* **2015**, *576*, 49.

[110] Y.-X. Mi, S. Wang, X.-X. Xu, H.-Q. Zhao, Z.-B. Zheng, X.-L. Zhao, Y.-X. Mi, S. Wang, X.-X. Xu, H.-Q. Zhao, Z.-B. Zheng, X.-L. Zhao, *J. Chil. Chem. Soc.* **2019**, *64*, 4392.

[111] C. Bailly, J. B. Chaires, *Bioconjugate Chem.* **1998**, *9*, 513.

[112] T.-P. Chiu, S. Rao, R. S. Mann, B. Honig, R. Rohs, *Nucleic Acids Res.* **2017**, *45*, 12565.

[113] D. Y. Lando, E. N. Galyuk, C.-L. Chang, C.-K. Hu, *J. Inorg. Biochem.* **2012**, *117*, 164.

[114] D. Y. Lando, C.-L. Chang, A. S. Fridman, I. E. Grigoryan, E. N. Galyuk, Y.-W. Hsueh, C.-K. Hu, *J. Inorg. Biochem.* **2014**, *137*, 85.

[115] A. S. Fridman, V. Brabec, S. G. Haroutiunian, R. M. Wartell, D. Y. Lando, *J. Biomol. Struct. Dyn.* **2003**, *20*, 533.

[116] H. Rozenberg, D. Rabinovich, F. Frolow, R. S. Hegde, Z. Shakked, *Proc. Natl. Acad. Sci. U.S.A.* **1998**, *95*, 15194–15199.

[117] H. Song, J. T. Kaiser, J. K. Barton, *Nat. Chem.* **2012**, *4*, 615.

[118] S. A. Hollingsworth, R. O. Dror, *Neuron* **2018**, *99*, 1129.